Aerodynamic Design Optimization Studies of a Blended-Wing-Body Aircraft

Zhoujie Lyu* and Joaquim R. R. A. Martins†

University of Michigan, Ann Arbor, Michigan 48109

The blended wing body is an aircraft configuration that has the potential to be more efficient than conventional large transport aircraft configurations with the same capability. However, the design of the blended wing is challenging due to the tight coupling between aerodynamic performance, trim, and stability. Other design challenges include the nature and number of the design variables involved, and the transonic flow conditions. To address these issues, a series of aerodynamic shape optimization studies using Reynolds-averaged Navier–Stokes computational fluid dynamics with a Spalart–Allmaras turbulence model is performed. A gradient-based optimization algorithm is used in conjunction with a discrete adjoint method that computes the derivatives of the aerodynamic forces. A total of 273 design variables — twist, airfoil shape, sweep, chord, and span — are considered. The drag coefficient at the cruise condition is minimized subject to lift, trim, static margin, and center plane bending moment constraints. The studies investigate the impact of the various constraints and design variables on optimized blended-wing-body configurations. The lowest drag among the trimmed and stable configurations is obtained by enforcing a 1% static margin constraint, resulting in a nearly elliptical spanwise lift distribution. Trim and static stability are investigated at both on- and off-design flight conditions. The single-point designs are relatively robust to the flight conditions, but further robustness is achieved through a multipoint optimization.

I. Introduction

FUEL has become the largest contributor to the direct operating costs of airlines; the fuel cost per passenger-mile more than doubled from 2001 to 2010.‡ Research in aircraft design is therefore placing an increasing emphasis on fuel burn reduction. One of the most promising ways to reduce fuel burn is to use an unconventional aircraft configuration. Unconventional aircraft configurations, such as the blended wing body (BWB), have the potential to significantly reduce the emissions and noise of future large transport aircraft [1].

The BWB configuration, also known as the hybrid wing body, is characterized by an airfoil-shaped centerbody that integrates payload, propulsion, and control surfaces. Compared to the classic tube-and-wing configuration, the BWB has superior aerodynamic performance [1–3]: the reduction in the wetted area substantially reduces the skin friction drag; the all-lifting design reduces the wing loading and improves the spanwise lift distribution; the smooth blended wing centerbody intersection reduces the interference drag; and the area-ruled shape of the BWB reduces the wave drag at high transonic speed. The centerbody provides a substantial portion of the total lift, thus reducing the wing loading. The low wing loading ensures excellent low-speed flight characteristics as well, making heavy high-lift mechanisms, such as double-slotted flaps, redundant. The cross-sectional area of the BWB is similar to that of the Sears–Haack body, which results in lower wave drag at transonic speeds, according to Whitcomb's area rule [4]. However, the design of BWB configurations introduces new challenges.

The main problem is that, because the BWB does not have a horizontal tail, the pressure distributions over the centerbody and wings must be carefully designed to maintain trim and the desired static margin. The thick airfoil shape of the centerbody also makes it a challenge for the BWB to achieve low drag while generating sufficient lift at a reasonable deck angle. Thus, there are critical tradeoffs between aerodynamic performance, trim, and stability.

Several authors have investigated the design optimization of the BWB configuration. Liebeck [1,5] and Wakayama [6,7] presented the multidisciplinary design optimization (MDO) of the Boeing BWB-450. They used a vortex-lattice model and monocoque beam analysis, and they also considered the trim and stability of the BWB. Qin et al. [3,8] performed an aerodynamic optimization of the European Multidisciplinary Optimization BWB (MOB) geometry, including inverse design and three-dimensional (3-D) shape optimization with a trim constraint. They optimized the design in three dimensions using Euler-based computational fluid dynamics (CFD). Peigin and Epstein [9] used a genetic algorithm and reduced-order methods to perform a multipoint drag minimization of the BWB with 93 design variables. They used a full Navier–Stokes analysis with reduced-order methods. Kuntawala [10] and Kuntawala et al. [11] studied BWB planform and shape drag minimization using Euler CFD with an adjoint implementation. Meheut et al. [12] performed a shape optimization of the AVECA flying wing planform subject to a low-speed takeoff rotational constraint. They optimized a total of 151 design variables, and they used CFD with a frozen-turbulence Reynolds-averaged Navier–Stokes (RANS) adjoint to compute the gradient.

Mader and Martins [13] studied the Euler-based shape optimization of a flying wing considering trim, bending moment constraints, and both static and dynamic stability constraints. Using a minimum induced-drag planform as a reference, they studied the effect of the various constraints on the optimal designs. Their results showed that, at subsonic and moderate transonic speeds, the static constraints can be satisfied with airfoil shape variables alone using a reflex airfoil. However, at high transonic speeds, or when considering dynamic stability constraints, the optimal designs required sweep, twist, and airfoil shape variables to minimize the drag while satisfying the constraints. Lyu and Martins [14] investigated the BWB shape optimization with bending moment, trim, and static margin constraints using Euler CFD, including planform optimization. They followed this with a similar study that used a RANS solver [15], which provided the basis for the present study. Reist and

Zingg [16] studied the aerodynamic shape optimization of a short-range regional BWB with Euler CFD.

What is missing is a comprehensive and systematic study of a BWB configuration that investigates the design tradeoffs between aerodynamic performance, trim, stability, as well as structural considerations, with appropriate fidelity. In this case, the appropriate fidelity is RANS CFD: whereas Euler-based optimization can provide design insights, the resulting optimal shapes are significantly different from those obtained with RANS, and Euler-optimized shapes tend to exhibit nonphysical features, such as a sharp pressure recovery near the trailing edge [17].

The objective of the present work is to develop a methodology for the aerodynamic design of BWB configurations that performs optimal tradeoffs between the performance and constraints mentioned earlier, and to examine the impact of each constraint on optimal designs. We investigate the design tradeoffs by performing a series of aerodynamic shape and planform optimization studies that examine the impact of the design variables and constraints. We explore the effect of the trim constraint, bending moment (BM) constraint, required static margin, and center-of-gravity (CG) location on the BWB optimal shape. We also investigate the impact of multipoint design optimization. This work extends our preliminary studies to multipoint RANS-based aerodynamic shape and planform optimization [15].

The paper is organized as follows. The numerical tools used in this work are described in Sec. II. The problem formulation, the mesh, and the baseline geometry are discussed in Sec. III. Finally, the series of aerodynamic design optimization cases is presented and discussed in Sec. IV, followed by the Conclusions.

II. Methodology

This section describes the numerical tools used. These tools are components of the MDO for Aircraft Configurations with High fidelity (MACH) [18,19]. MACH can perform the simultaneous optimization of aerodynamic shape and structural sizing variables considering aeroelastic deflections. However, in this paper we focus solely on the aerodynamic shape optimization.

A. Geometric Parametrization

We use a free-form deformation (FFD) approach to parametrize the geometry [20]. The FFD volume parametrizes the geometry changes rather than the geometry itself, resulting in a more efficient and compact set of geometry design variables, and thus making it easier to handle complex geometric manipulations. Any geometry may be embedded inside the volume by performing a Newton search to map the parameter space to physical space. All the geometric changes are performed on the outer boundary of the FFD volume. Any modification of this outer boundary can be used to indirectly modify the embedded objects. The key assumption of the FFD approach is that the geometry has constant topology throughout the optimization process, which is usually the case for wing design. In addition, because FFD volumes are trivariate B-spline volumes, the sensitivity information of any point inside the volume can be easily computed. Figure 1 shows the FFD volume and geometric control points for the BWB aerodynamic shape optimization.

To trim the BWB configuration, we use control surfaces on the rear centerbody, which are analogous to elevators on a conventional configuration. A nested FFD volume is used to implement the movement of these control surfaces, as shown in Fig. 1. The result is a sub-FFD that is embedded in the main FFD. Any changes in the main FFD are propagated to the sub-FFD. The sub-FFD is set to rotate about the hinge line of the control surface. When the sub-FFD rotates, the embedded geometry changes the local shape accordingly. Because of the constant topology assumption of the FFD approach, and the limitation of the mesh perturbation, the surface has to be continuous around the control surfaces, eliminating the elevator gap. Therefore, when the control surfaces deflect, there is a transition region between the control surface and the centerbody, similar to those studied in a continuous morphing wing [21]. Figure 2 shows the sub-FFD volume and the geometry, with a trim control surface deflection of 25 deg.
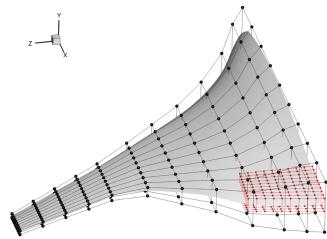

Fig. 1   FFD volume and control surface sub-FFD volume with their respective control points.
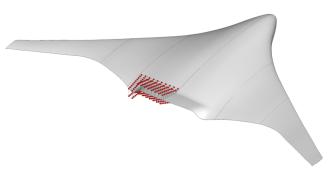

Fig. 2   Sub-FFD volume and control points for a trim control surface deflection of 25 deg.

B. Mesh Perturbation

Because FFD volumes modify the geometry during the optimization, we must perturb the mesh for the CFD analysis to solve for the modified geometry. The mesh perturbation scheme used in this work is a hybridization of algebraic and linear elasticity methods [20]. The idea behind the hybrid warping scheme is to apply a linear-elasticity-based warping scheme to a coarse approximation of the mesh to account for large, low-frequency perturbations, and to use the algebraic warping approach to attenuate small, high-frequency perturbations. The goal is to compute a high-quality perturbed mesh similar to that obtained using a linear elasticity scheme but at a much lower computational cost.

C. CFD Solver

We use the Stanford University multiblock (SUmb) [22] flow solver. SUmb is a finite-volume, cell-centered multiblock solver for the compressible Euler, laminar Navier–Stokes, and RANS equations (steady, unsteady, and time periodic). It provides options for a variety of turbulence models with one, two, or four equations and options for adaptive wall functions. The Jameson–Schmidt–Turkel scheme [23] augmented with artificial dissipation is used for the spatial discretization. The main flow is solved using an explicit multistage Runge–Kutta method along with a geometric multigrid scheme. A segregated Spalart–Allmaras (SA) turbulence equation is iterated with the diagonally dominant alternating direction implicit method. An automatic differentiation adjoint for the Euler and RANS equations was developed to compute the gradients [17,24]. The adjoint implementation supports both the full-turbulence and frozen-turbulence modes, but in the present work we use the full-turbulence adjoint exclusively. The adjoint equations are solved with preconditioned generalized minimal residual method (GMRES) [25] using PETSc [26,27].[§]

[§]Data available online at http://www.mcs.anl.gov/petsc [retrieved 18 June 2013].

D. Optimization Algorithm

Because of the high computational cost of CFD solutions, it is critical to choose an efficient optimization algorithm that requires a reasonably low number of function calls. Gradient-free methods, such as genetic algorithms, have a higher probability of getting close to the global minimum for cases with multiple local minima. However, slow convergence and the large number of function calls make gradient-free aerodynamic shape optimization infeasible with the current computational resources, especially for large numbers of design variables. Therefore, we use a gradient-based optimizer combined with adjoint gradient evaluations to solve the problem efficiently.

We use sparse nonlinear optimizer (SNOPT) [28] through the Python interface pyOpt [29] for all the optimizations presented here. SNOPT is a gradient-based optimizer that implements a sequential quadratic programming method; it is capable of solving large-scale nonlinear optimization problems with thousands of constraints and design variables. SNOPT uses a smooth augmented Lagrangian merit function, and the Hessian of the Lagrangian is approximated using a limited-memory quasi-Newton method.

III. Problem Formulation

The BWB configurations can have significantly better aerodynamic performance than conventional configurations do. To fully realize this potential, however, the external shape of the BWB has to be carefully designed. The primary focus of this study is drag minimization subject to a lift constraint. In addition, we consider the following constraints: trim, static margin, and bending moment. In this section, we discuss the problem setup and the optimization formulation for the aerodynamic shape optimization of the BWB.

A. Initial Geometry

The initial geometry is shown in Fig. 3. The BWB geometry has a similar planform shape to the first-generation Boeing BWB design with 800 passengers [1]. This geometry has a span of 280 ft and a total length of 144 ft; it is divided into a centerbody section and an outer wing section. Based on this planform, the mean aerodynamic chord (MAC) is 86 ft. The initial CG is at 40% MAC of the planform. The placement of the CG is studied in Sec. III.C.

The geometry is generated with a prescribed thickness-to-chord ratio (t/c), 18% at the center plane and 10% at the tip, as well as prescribed leading edge (LE) and trailing edge (TE) locations. We use the NASA SC(2)-0518 airfoil at the center plane and the NASA SC

Table 1 Geometric parameters for the BWB

Geometric parameter	Baseline BWB
Span	280 ft
Length	144 ft
Reference area	15, 860 ft^2
Mean aerodynamic chord	86 ft

(2)-0410 airfoil at the tip, and we quadratically interpolate the airfoil sections in between. Table 1 summarizes the geometric parameters of the baseline BWB. The reference area is the actual area of the whole planform.

B. Grid Convergence Study

We generate the mesh for the BWB using an in-house hyperbolic mesh generator. The mesh is matched out from the surface mesh with an O-grid topology. The nominal cruise flow condition is Mach 0.85 at 35,000 ft, and the Reynolds number is 100 million based on MAC. The spacing on the first layer uses a y^+ of 0.5 to adequately resolve the boundary layer. The grid is matched out to a far field that is located at a distance of 25 times the span, with an average growth ratio of 1.2. The grid used for the optimization has 2.92 million cells. It is generated from a surface mesh with 120 spanwise cells and 120 chordwise cells on each surface. There are also additional cells for the finite TE thickness and the rounded wingtip, resulting in a total of 30,464 surface cells. The resulting O-grid has 96 cells in the k direction.

We perform a grid convergence study to determine the resolution accuracy of this grid. All the grids are generated using the hyperbolic mesh generator with a coarse or refined spacing. Figure 4 shows the mesh convergence plot, showing that the result for the mesh with 2.92 million cells is within three drag counts of that for the mesh with 187 million cells. We choose the former grid because it allows a reasonable optimization run time while providing sufficient accuracy. The RANS flow solution can be obtained within 100 min from a cold start with six orders of residual reduction on 180 processors. Figure 5 shows the BWB mesh on the surface and the symmetry plane.

C. Optimization Problem Formulation

1. Objective Function

For the optimization studies, we minimize the drag coefficient at the nominal cruise condition, subject to a lift coefficient constraint.
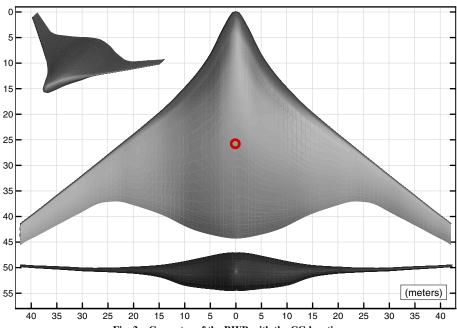

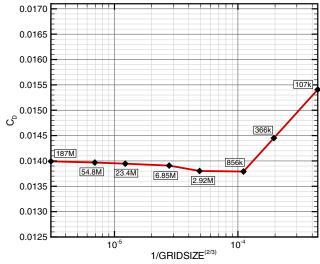**Fig. 3 Geometry of the BWB with the CG location.**

Fig. 4   Mesh convergence plot of the initial BWB mesh at nominal cruise condition.
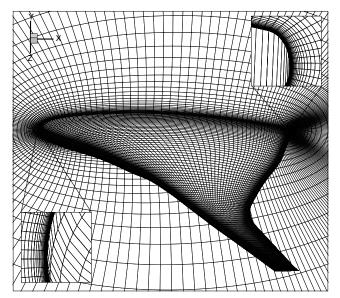

Fig. 5   BWB mesh showing surface and center plane cells.

The drag coefficient is given by the RANS solutions. The cruise lift coefficient is constrained to $C_L = 0.206$. The chosen C_L is similar to that of the first-generation Boeing BWB [1], assuming a cruise altitude of 35,000 ft and a cruise Mach of 0.85. Because both the lift and drag coefficients use the whole planform area as the reference area, this results in a lower wing loading and lift coefficient.

2.   Design Variables

The first set of design variables consists of control points distributed on the FFD volume. A total of 240 shape variables is distributed on the lower and upper surfaces of the FFD volume, as shown in Fig. 1. The large number of shape variables provides more degrees of freedom for the optimizer to explore, and this allows us to fine-tune the sectional airfoil shapes and the thickness-to-chord ratios at each spanwise location. Because of the efficient adjoint implementation, the cost of computing the shape gradients is nearly independent of the number of shape variables [18].

The next set of design variables is the spanwise twist distribution. We use 10 sectional twist design variables. The center of the twist rotation is fixed at the reference axis, which is located at the quarter chord of each section. The twist variables provide a way for the optimizer to minimize induced drag by controlling the spanwise lift

distribution and a way to satisfy the center plane bending moment constraint.

We also consider planform variables, which can contribute to the reduction of wave drag. The sweep angle, chord length, and width of the centerbody are kept constant; only the planform variables of the outer wing are used as design variables. The outer wing is defined as the outer 60% of the total span, where the wing-centerbody blending region ends. The outer wing is divided into seven sections. Each section has an independent set of planform variables, which are the sweep angle, chord length, and span of the section. Table 2 and Fig. 6 list the design variables. By providing complete freedom of the outer wing, we allow the optimizer to explore the optimal planform shape.

At the conceptual and preliminary design stages, the CG location should be optimized subject to trim and longitudinal stability constraints to minimize the trim drag. Thus, we use the CG location as a design variable that is allowed to move between 30% MAC and 50% MAC. In our case this variable represents the CG of the centerbody and the associated systems and payload. The CG of the wings is considered separately and is a function of the wing planform shape.

We add some auxiliary design variables to facilitate the formulation of the optimization problem. The angle-of-attack variable ensures that the lift coefficient constraint can be satisfied. We use an individual design feasible (IDF) approach [30] to update MAC. This requires the addition of a target variable and a compatibility constraint. With the IDF approach, the geometry manipulation and computation of MAC can be decoupled from the aerodynamic solver. Therefore, the sensitivity of MAC is also decoupled from the aerodynamic solver, which significantly simplifies the optimization problem formulation.

3.   Constraints

Because optimizers tend to explore any weaknesses in numerical models and problem formulations, an optimization problem needs to be carefully constrained in order to yield a physically feasible design. We implement several geometric constraints. First, we impose thickness constraints from the 5% chord at the LE to the 95% chord near the TE. A total of 400 thickness constraints is imposed in a 20 by 20 grid. The constraints have a lower bound of 70% of the baseline thickness and no upper bound. These constraints ensure sufficient height in the centerbody cabin and sufficient fuel volume. The LE thickness constraint allows for the installation of slats, and the TE thickness is limited due to manufacturing constraints.

The total volume of the centerbody and the wing is also constrained to meet the volume requirements for the cabin, cargo, and systems, as well as fuel. The LE and TE shape variables are constrained such that each pair of shape variables on the LE and TE can move only in opposite directions with equal magnitudes, so that twist cannot be generated with the shape design variables. Instead, twist is implemented as a separate set of variables.

Because of the absence of a structural model, we use the bending moment at the center plane as a surrogate for the structural weight trade-off and to prevent unrealistic spanwise lift distributions and wing spans. This bending moment is constrained to be less than or equal to the baseline bending moment. The bending constraint is necessary to capture the tradeoffs between aerodynamic performance and structural weight. However, it is possible to perform these

Table 2   Design variables for the BWB aerodynamic shape optimization

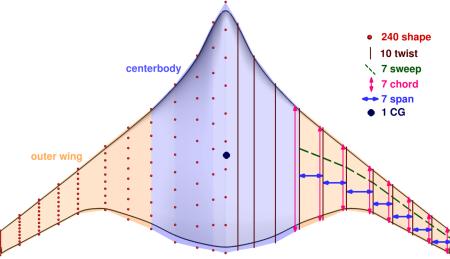| Design variable	Count
Shape	240
Twist	10
Sweep	7
Chord	7
Span	7
Angle of attack	1
MAC^t	1
Total	**273**

Fig. 6   Shape and planform design variables.

tradeoffs with more accuracy by using high-fidelity aerostructural optimization, as done by Kenway and Martins [19].

In addition, the BWB has to be trimmed at each flight condition. Ideally, the aircraft is trimmed at the nominal cruise condition without requiring control surface deflection. Therefore, we freeze the sub-FFD, which rotates the trim control surface during the on-design optimization with the pitching moment constraint. The sub-FFD is then used in the analysis of off-design conditions. There are several ways to trim a flying wing: by unloading wingtip on a swept wing, by adding reflex to the airfoils at the TE, or a combination of both of these [13]. Our optimization problem has all the required degrees of freedom to meet the trim constraint.

Longitudinal stability is also a particularly important design consideration for the BWB configuration. With the absence of a conventional empennage, it is not immediately obvious how to best achieve a positive static margin for a BWB aircraft. The goal is to maintain a positive static margin for all flight conditions. We constrained the static margin to be greater than 1%. The static margin K_n can be calculated as the ratio of the moment and lift derivatives [31,32]:

$$K_n = -\frac{C_{M_\alpha}}{C_{L_\alpha}} \qquad (1)$$

We calculate C_{M_α} and C_{L_α} using finite differences with an angle of attack step size of 0.1 deg. The static margin constraint incurs an additional computational cost. For each iteration, one additional flow solution and two additional adjoint solutions are required. Both the flow and adjoint solutions have to be converged more accurately than usual to obtain an accurate static margin gradient. This is particularly important for static margin gradients with respect to shape variables because they have relatively small magnitudes compared to other gradients.
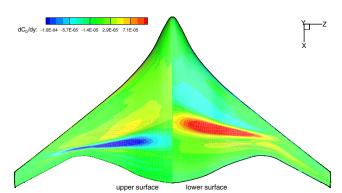

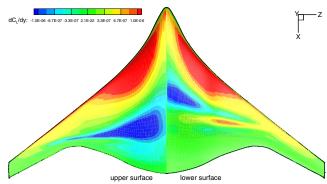**Fig. 7   Study 0: dC_D/dy contour of the baseline BWB.**

Fig. 8   Study 0: dC_L/dy contour of the baseline BWB.

Table 3 summarizes the constraints for the optimization problems. All constraints are implemented as nonlinear constraints in the SNOPT optimizer.

D.   Study 0: Baseline Optimization

To achieve a reasonable comparison for the optimization studies, we perform a baseline optimization by minimizing drag with respect to the spanwise twist distribution subject to a lift constraint. The airfoil profiles are the same as for the original geometry. The improved baseline has a drag nine counts lower than that of the untwisted baseline. The studies in Sec. IV use this improved baseline as the initial starting geometry for the optimization.

The improved baseline can still be improved upon, especially through changes in the sectional airfoil shape. The sensitivity of the

Table 3   Summary of the constraints used in the BWB aerodynamic shape optimization

Constraint	Count	Type
Thickness	400	$\leq$
LE, TE control points	40	$\leq$
Lift coefficient	1	$=$
Trim	1	$=$
Internal volume	1	$\leq$
Static margin	1	$\leq$
MAC compatibility	1	$=$
Total	445	

drag and lift with respect to the airfoil shape can be visualized through a sensitivity contour plot, shown in Figs. 7 and 8. Here, we plot the derivatives of C_D and C_L with respect to shape variations in the y direction. The regions with the highest gradient of C_D are near the shock on the upper and lower surfaces. This indicates that shock reduction through local shape changes is the major driver in reducing C_D at the beginning of the optimization. As for C_L, a high positive gradient is observed near the LE, indicating that moving in the positive y direction increases C_L. A high negative derivative is observed in the aft of the centerbody, indicating that moving the aft portion in the negative y direction increases C_L.

In addition, the regions with high derivative values on the lower and upper surfaces are offset longitudinally, which suggests that airfoil camber on the centerbody can further increase C_L. However, these sensitivity plots are only a linearization about the current design point, and they provide no information about the constraints. Nonetheless, these sensitivity plots indicate what drives the design at this design point.

IV.   Aerodynamic Design Optimization Studies

We perform a series of RANS-based aerodynamic shape optimizations to examine the effects of various selections of design variables and constraints. The gradient-based optimizer (SNOPT) is used with sensitivities computed by the adjoint method. The full turbulence adjoint used includes the linearization of both the main flow solver and the SA turbulence model. The optimizations are converged to an optimality tolerance of $\mathcal{O}(10^{-5})$. By combining different sets of design variables and constraints, we explore the tradeoffs and benefits of each. The initial design point for all the optimizations is the twist-optimized baseline described earlier. We then progress by adding airfoil shape variables (Study 1), a trim constraint (Study 2), a CG position variable and static margin constraint (Study 3), a bending moment constraint (Study 4), and planform design variables (Study 5). Finally, we consider multipoint optimization (Study 6). This series of optimization studies allows us to examine how the optimization problem formulation impacts the practical design optimization of the BWB.

The optimizations are performed using the Advanced Research Computing cluster at the University of Michigan. Each computing node in this cluster has two six-core 2.67 GHz Intel Xeon X5650 processors per node. Each node has a total of 48 GB RAM. The cluster uses InfiniBand networking for interconnections.

A.   Study 1: Shape and Twist Design Variables

In this first study, we add airfoil shape design variables to the twist variables already considered in the baseline optimization. A total of 240 shape design variables is used to optimize the airfoil shape. As shown in Fig. 6, 12 airfoil sections are equally distributed in the spanwise direction. Each section has 10 control points on the upper surface and 10 control points on the lower surface. The angle of attack is also allowed to change during the optimization. The CG is fixed at 40% MAC. Only lift and geometry constraints are imposed. Therefore, one flow solution and two adjoint solutions are needed at each iteration. The optimization converged in 10 h using 240 processors; the convergence history of the optimization is shown in Fig. 9.

Without any additional constraints, we expect to see a lift distribution that is close to elliptical, along with weakened shocks. Figure 10 shows the pressure distribution, twist, sectional airfoil shape, shock surface, and lift distribution of the twist-optimized baseline and the optimized BWB for Study 1. A hypothetical elliptical lift distribution is shown in gray. We compute the shock surface from the volume solution grid by constructing an isosurface of the normal Mach number [33]. The shock occurs where the normal Mach number is one; that is,

$$M_n = \frac{\mathbf{u}}{a} \cdot \frac{\nabla p}{|\nabla p|} = 1 \qquad (2)$$
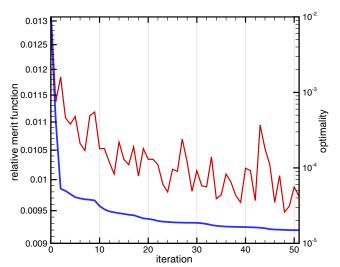

Fig. 9   Study 1: relative merit function and optimality history of the optimization.

The dimensions in the figures are normalized by the half span, $\eta_s = z/(b/2)$, and by chord, $\eta_c = x/c$.

As shown in the pressure distributions, the shape design variables make a significant contribution to the minimization of the drag. The baseline BWB exhibits a front of very closely spaced pressure contour lines spanning a significant portion of the wing, indicating a shock. The optimized BWB shows parallel pressure contour lines with roughly equal spacing, indicating a nearly shock-free solution at the nominal cruise condition. This is confirmed by the shock surface plots: we can see that the baseline BWB has a shock on the upper surface, whereas the optimized design has eliminated most of the shock at the design condition. The shock elimination can also be seen on the airfoil C_p distributions. At $\eta_s = 0.4$ and $\eta_s = 0.9$, the sharp increase in local pressure due to the shock becomes a gradual change from the LE to the TE. The magnitude of C_p is also lowered near the LE.

The optimized lift distribution is much closer to the optimal elliptical lift distribution. This is achieved by altering the twist distribution. The highest twist is near the Yehudi break at $\eta_s = 0.6$, where the strong shock occurred on the baseline BWB. The drag coefficient is decreased by 39 counts. The twist angle at this section is increased to 5 deg. The fact that the twist distribution has changed so much relative to a geometry that was already optimized for twist emphasizes the importance of simultaneously optimizing the twist and the airfoil shapes.

The angle of attack changed slightly from −0.4 to −1.0 deg. Because the CG is fixed at 40% MAC, the static margin is changed only by the shift in the aerodynamic center. The optimized design has reduced the static margin from 10.4 to 3.7%. A detailed study of the CG placement and static margin is presented in Sec. IV.C.

To study the effect of the twist variables, we performed a separate optimization that optimized only for the airfoil shape variables and did not include the twist design variables. The pressure distribution and airfoil profiles were similar to those for the case where both twist and airfoil shape were optimized. As shown in Table 4, the penalty for not including the twist variables is only 1.4 counts. Note, however, that we always start the optimization with the twist-optimized baseline geometry. Because the total variation of the optimized twist distribution is less than 5 deg, the airfoil shape variables are able to get close to the overall optimum. Note that only aerodynamic performance is considered in this study. Other considerations, such as stall speed or wing structure, would pose additional constraints on the twist distribution.

B.   Study 2: Trim Constraint

In this study, we investigate the effect of a trim constraint with a fixed CG. The formulation is the same as that of the preceding
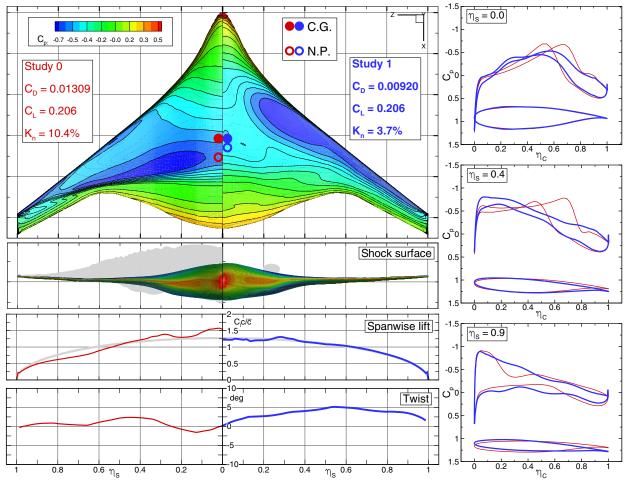
Fig. 10   Study 1: the optimized design reduced drag by 30% compared to the baseline.

study, with the addition of a trim constraint. Trim drag is more of a design driver in the BWB than in conventional tube-and-wing configurations because elevator trim affects the flow around the BWB centerbody. Trim is also coupled to the longitudinal stability. Figure 11 shows the pressure distribution, twist, sectional airfoil shape, shock surface, and lift distribution of the optimized BWB for studies 1 and 2.

The overall pressure contour is similar to that of Study 1. Compared to Study 1, the upper surface shock has increased at the optimum. However, it is still less severe than that of the baseline. The twist angles on both the centerbody and the outer wing are reduced. The wing has nearly zero twist for a large portion of the outer wing. The wingtip has a negative twist of 3 deg (washout) in order to satisfy the trim constraint. Two design features helped satisfy the trim constraints of the optimized BWB. The first is a reflex near the TE throughout most of the span, resulting in a significant change to the chordwise pressure distribution. Most lift is generated at the forward section of the wing, whereas the aft section has significantly less lift to trim the aircraft. Therefore, the net lift near the tip is reduced. The second feature is the unloaded wingtip. The optimized wingtip airfoil has washout and less lift than that of Study 1. The unloaded wingtip

on a highly swept wing acts as a horizontal tail to trim the aircraft. Because of the trim constraint, the optimized drag coefficient is five counts higher than that of the preceding study. This change is primarily due to a lower span efficiency and the reflex in the TE.

To investigate the off-design conditions, we perform a Mach sweep from 0.6 to 0.875. We use a sub-FFD to deflect the control surface near the rear centerbody to trim the aircraft at each condition, as shown in Fig. 1. The results are compared with the twist-optimized baseline design in Fig. 12. By comparing the trimmed baseline and optimized designs, we see that a trimmed drag pocket is achieved in the transonic region from Mach 0.80 to 0.86. The baseline design starts the drag rise near Mach 0.80, whereas the optimized design significantly delays the drag rise. The drag coefficient of the optimized design remains nearly constant up to Mach 0.86.

In addition, by comparing the trimmed and untrimmed results, we can quantify the trim drag at each condition. Figure 13 shows the trim drag of the baseline and optimized BWB. We see that the baseline design has lower trim drag at low Mach numbers. The optimized design, however, reverses this trend, and the trim drag reduces with increasing Mach number up to the design Mach number. Although this is a point design, the trim drag is relatively insensitive to the Mach number around the design point.

C. Study 3: CG Design Variable and Static Margin Constraint

In the preceding study, we examined the trim constraint with a fixed CG location. At the conceptual design stage, the CG can often be changed by moving systems, fuel, engines, and payload. By allowing the CG to change within a given range, we may discover additional benefits. To investigate the effect of CG location, we performed the same optimization as in Study 2 at various CG
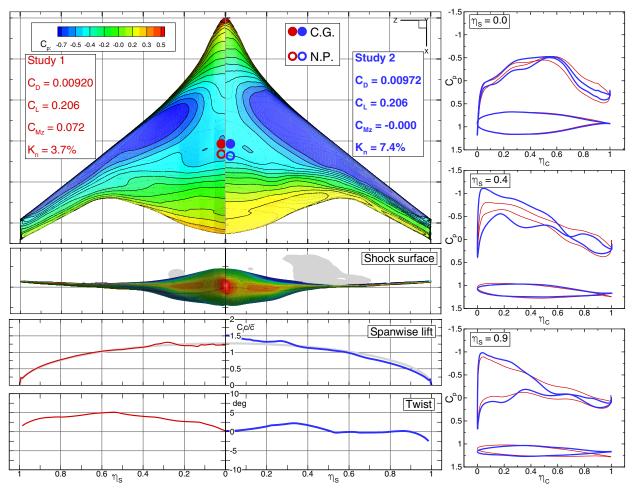
Table 4   Study 1: Comparison of twist design variables

Coefficient	C_D	C_L
Baseline	0.01309	0.206
Twisted optimum	0.00920	0.206
Fixed twist optimum	0.00934	0.206

Fig. 11   Study 2: the trim constraint imposes 5 drag count penalty.
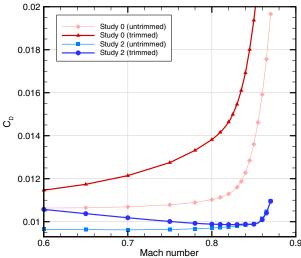

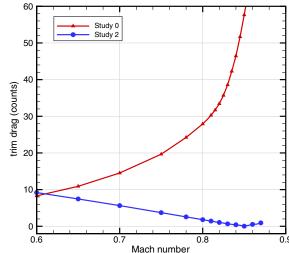**Fig. 12   Mach sweep of trimmed and untrimmed designs for studies 0 and 2.**

Fig. 13   Trim drag of optimized BWB for studies 0 and 2.

locations: 30, 40, and 50% MAC. The results are summarized in Table 5.

Both the drag coefficient and the static margin are strongly affected by the CG location. Because a lower trim moment is required for an aft CG location, the trim constraint tends to move the CG aft. We see that as the CG moves aft, the drag coefficient decreases, and the amount of reflex and washout is reduced. As the CG moves aft, the static margin decreases. For a flying wing, the location of the NP

Table 5   Study 3: comparison of drag and static margin for varying CG position

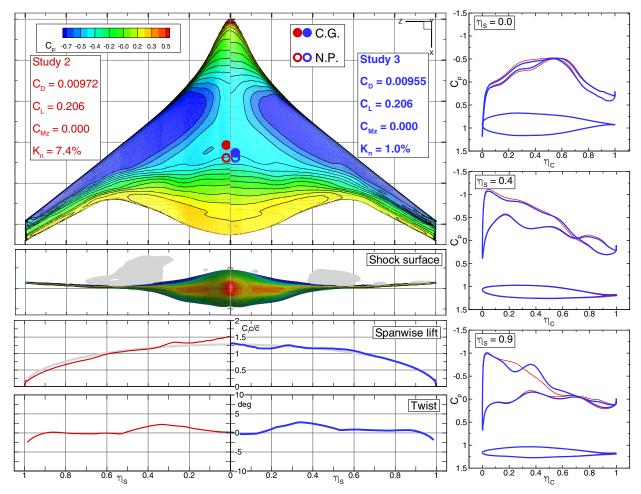| CG position	C_D	K_n, %
30% MAC	0.01032	19.6
40% MAC	0.00972	7.4
50% MAC	0.00941	−1.8

Fig. 14   Study 3: 1% static margin is achieved with the CG design variable.

coincides with the aerodynamic center. For a fixed planform, the aerodynamic center varies only slightly with the airfoil shape variables. Therefore, the resulting static margin of the optimized design varies nearly linearly with the CG location.

Because the CG location is limited by both the trim and static margin, the problem formulation with CG design variables is a well-posed optimization problem. Simply adding CG design variables alone would result in the CG being as far aft as possible. Therefore, the CG design variable has to be added in conjunction with the static margin constraint. We perform another optimization with the CG position as a design variable and a static margin constraint. The CG is allowed to vary between 30 to 50% MAC. The static margin constraint has a lower bound of 1%.

This optimization problem is more computationally intensive than the preceding cases for two reasons. First, each iteration requires two flow solutions and six adjoint solutions to obtain the static margin and its gradient. Second, the static margin gradient is a second-order derivative because it is the gradient of the lift and moment coefficient gradients. Therefore, to achieve an accurate static margin gradient, both the flow and adjoint solutions must be converged to a higher tolerance, $\mathcal{O}(10^{-8})$. Figure 14 shows the pressure distribution, twist,
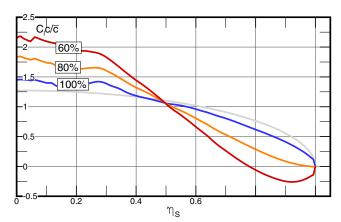

Fig. 15   Study 4: spanwise lift distribution of optimized designs with various levels of bending moment constraint.

sectional airfoil shape, shock surface, and lift distribution of the optimized BWB for studies 2 and 3.

The overall pressure contours and airfoil profiles are similar to those for the optimal shape in the preceding study. At the optimum, CG moves from 40% MAC to 47% MAC, driven by the trim constraint. Compared to Study 2, less airfoil reflex and wingtip unloading are needed to trim the BWB, resulting in an additional reduction of 1.7 in the drag count. The static margin is driven to the lower bound of 1%. In this study, CG is optimized based only on the aerodynamic performance and longitudinal stability. In reality, additional factors must be considered, such as the aircraft systems

Table 6   Study 4: Comparison of optimized aerodynamic coefficients at various bending moment constraints

Coefficient	C_D	C_{BM}
100% BM	0.00961	0.131
80% BM	0.01103	0.105
60% BM	0.01399	0.078

placement and the CG movement during operation, but these are beyond the scope of this study.

D. Study 4: Bending Moment Constraint

During the optimization, the aerodynamic load shifts. This may result in an increase in the structural stresses, which would impact the structural weight and thus the overall aircraft performance. A full aerostructural optimization, such as that presented by Kenway and Martins [19], is beyond the scope of this work, but to limit the impact of the aerodynamic optimization on the structural weight, we add a center plane bending moment constraint [34]. This study is identical to Study 1 except for the addition of the bending moment constraint. The bending moment is taken about the center plane of BWB. We perform a series of optimizations with various bending moment constraints. The bending moment is constrained to be less than 100, 80, or 60% of the bending moment of the twist-optimized baseline. The results are summarized in Table 6.

The addition of bending moment constraints drives the lift distribution away from elliptical. Figure 15 shows the lift distributions for each value of the bending moment constraint. A hypothetical elliptical span loading with the same lift is shown in gray. The optimization with the 100% bending moment constraint achieves a lift distribution that is the closest to elliptical. As the bending moment constraint decreases, more lift is shifted inboard to achieve the same lift with a reduced bending moment. A 20% reduction in the center plane bending moment results in a 14.2 increase in the drag count. A 40% bending moment reduction incurs a 43.8 increase in the drag count. At the reduced bending moment, the wingtip generates negative lift to alleviate the bending moment. Thus, we see that the impact of the bending moment constraint on

aerodynamic performance is significant. For a careful tradeoff between aerodynamics and structure, we would need to optimize both the aerodynamic shape and the structural sizing considering both the cruise performance and multiple load conditions [19].

E. Study 5: Planform Design Variables

In this study, we add planform variables to the preceding study, which includes bending moment and trim constraints. The center-body planform shape is kept constant. As shown in Fig. 6, the outer wing is divided into seven sections. Each section has its own twist, chord, sweep, and span design variables. The change in the planform shape, especially the span variables, would result in a heavier structure if no bending constraint were imposed. The center plane bending moment is constrained to be less than or equal to that of the twist-optimized baseline. The CG is fixed at 40% MAC. The MAC and the reference area are recomputed at each iteration to take the planform variations into account. The resulting optimized design is shown in Fig. 16. The outline of the baseline planform is shown in red.

The sweep angles of the outer wing of the optimized planform decrease by 4 deg. Even with the degrees of freedom provided by the multiple sweep, span, and chord of the outer wing sections, the optimization achieves a straight LE on the wing toward the end of the optimization. Any intermediate LE kinks during the optimization are smoothed out toward the end. The span of the optimized BWB increases by 3%. A further increase in the span to reduce the induced drag is constrained by the center plane bending moment and the additional viscous drag due to the increase in the surface area. Because of the presence of the trim constraint, the wing airfoil has reflex near the TE, and the chordwise pressure distribution is similar to that of Study 2.
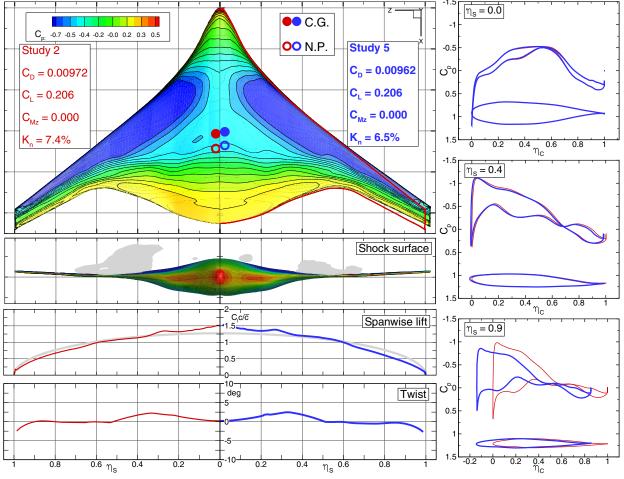

Fig. 16 Study 5: sweep angle is slightly reduced in planform optimization.

Table 7   Study 6: Flight conditions for the multipoint optimization

Flight condition	C_L	Mach
1	0.206	0.85
2	0.206	0.84
3	0.206	0.86
4	0.185	0.85
5	0.227	0.85

The planform study shows that the baseline is already relatively close to the optimal planform shape. Even with a marginal change in the planform, the additional degrees of freedom in the planform lead to a lower drag than the optimization with only shape variables. The drag reduces by an additional drag count compared to Study 2, while satisfying the bending moment constraint.

F. Study 6: Multipoint Optimization

Transport aircraft operate at multiple cruise conditions because of variability in both the missions and air traffic control restrictions. Single-point optimization at the nominal cruise condition could inflate the benefit of the optimization: it may improve the on-design performance while reducing the performance under off-design conditions. In this study, we investigate the impact of a multipoint optimization formulation on the optimized BWB design. To isolate the problem from other effects of the constraints, we choose to extend Study 1. The only difference is that the objective is now the average of the drag coefficients at multiple flight conditions. The flight conditions are the nominal cruise, $\pm 10\%$ of cruise C_L, and ± 0.1 of cruise Mach, as shown in Table 7. More sophisticated ways of

choosing multipoint flight conditions can be used, such as an automated selection of the points that minimize fleet-level fuel burn [35]. Figure 17 shows the multipoint optimized design at the nominal cruise condition. The multipoint optimized design is compared to the single-point optimum of Study 1.

The overall pressure distribution of the multipoint design is similar to that of the single-point design. The twist and lift distributions are nearly identical. Most of the differences are in the chordwise C_p distributions in the outer wing section. Because of the multipoint formulation, the nominal cruise condition has less authority over the shape changes. The drag coefficient of the multipoint optimum is two counts higher than that of the single-point optimum, and the shock surface is also larger. Because all the flight conditions are equally weighted, the optimizer trades off the drag between the multiple flight conditions.

To better understand the effects of multipoint optimization, we plot the ML/D contours of the baseline, single-point, and multipoint designs with respect to C_L and cruise Mach in Fig. 18. The line along which the aircraft is neutrally stable is shown in gray. ML/D provides a metric for quantifying aircraft range based on the Breguet range equation with constant thrust specific fuel consumption. Although the thrust specific fuel consumption is actually not constant, assuming it to be constant is acceptable when comparing range performance in a limited Mach number range [36].

The baseline maximum ML/D is at a lower Mach number and a higher C_L compared to the cruise flight condition. The single-point optimization significantly increases the maximum ML/D and the ML/D at the operation condition. In addition, the maximum ML/D occurs much closer to the nominal cruise condition. The shapes of the contours are also altered to move the maximum toward the cruise flight condition. For fixed $C_L = 0.206$, the maximum ML/D occurs
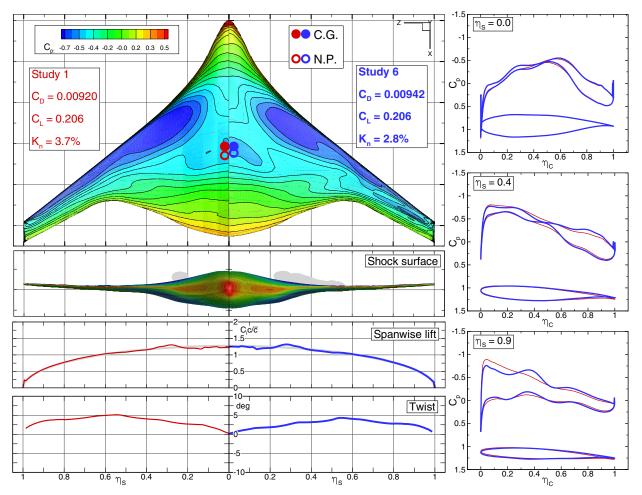

Fig. 17   Study 6: multipoint optimized design is 2 count higher at nominal flight condition.
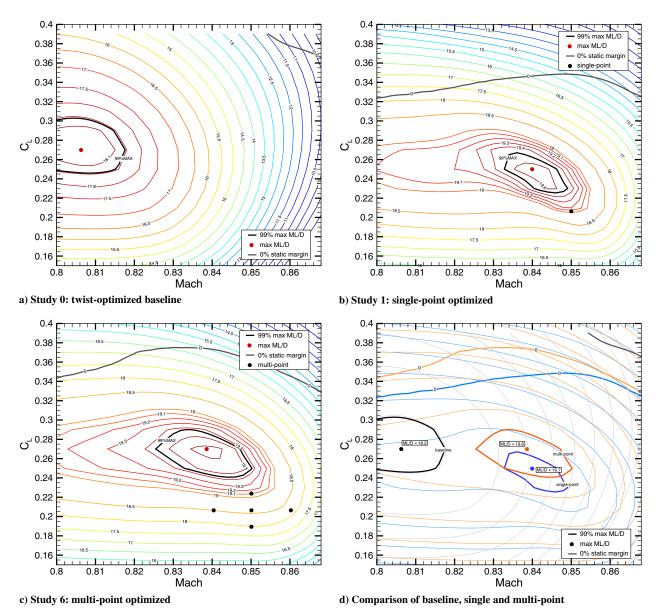
a) **Study 0: twist-optimized baseline**

b) **Study 1: single-point optimized**

c) **Study 6: multi-point optimized**

d) **Comparison of baseline, single and multi-point**

Fig. 18 **Study 6: multipoint optimization has an enlarged 99% ML/D contour.**

near a cruise Mach of 0.85, which is equivalent to the drag bucket in a drag divergence plot. For the multipoint optimization, the flight conditions for optimization are spread in the Mach, C_L space, resulting in a more flattened ML/D near the maximum. ML/D is more uniform near the operation flight conditions. The 99% ML/D contour is also larger than that of the single-point optimum. By examining the ML/D, we see that the C_L of the maximum ML/D is

still higher than the C_L in our optimization. An increase in the C_L may further improve the aerodynamic performance of the optimized BWB. The optimum C_L occurs between 0.25 and 0.27. Because the wing loading is constrained by the low speed performance, the only viable way to increase C_L for the BWB is to increase the cruise altitude. However, additional tradeoffs, such as cabin pressure and required thrust, must be taken into consideration.

Table 8   **Summary of the results of BWB aerodynamic design optimization studies**

Study	C_D	Design variables	CG, %	K_n, %	Geo	Lift	BM, %	Trim	K_n
0	0.01309	Twist	40	10.4	•	•			
1	0.00932	Shape	40		•	•			
	0.00920	Shape, twist	40	3.7	•	•			
2	0.01032	Shape, twist	30	19.6	•	•		•	
	0.00972	Shape, twist	40	7.4	•	•		•	
	0.00941	Shape, twist	50	−1.8	•	•		•	
3	0.00955	Shape, twist, CG	47	1.0	•	•		•	•
4	0.00961	Shape, twist	40		•	•	100%		
	0.01103	Shape, twist	40		•	•	80%		
	0.01399	Shape, twist	40		•	•	60%		
5	0.00962	Shape, twist, planform	40	6.5	•	•	100%	•	
6	0.00942	Shape, twist, multipoint	40	2.8	•	•			

V. Conclusions

A series of RANS-based aerodynamic shape optimization studies of a BWB configuration was presented to understand the tradeoffs between aerodynamic performance, and constraints on trim, stability, and bending moment. These studies also explored the effect of considering different sets of aerodynamic shape design variables (twist, airfoil shape, and planform shape) in the design optimization. Table 8 summarizes the results of the optimization studies.

The BWB configurations obtained in studies 0 and 1 had the lowest drag coefficient, but they are impractical because they are not trimmed. The airfoil shape design variables proved essential to the reduction of the shock on the upper surface and the wave drag associated with it. The enforcement of the trim constraint (Study 2) caused a 5.6% increase in drag. By moving the CG aft from 40% MAC to 50% MAC, this drag penalty was reduced to 2.3%, but resulted in a negative static margin (-1.8%).

Study 3 provides the best compromise between performance and stability by enforcing a small static margin that can be tolerated in a commercial airplane (1%) and including the CG position as a design variable. This resulted in a trimmed configuration that exhibits a nearly elliptical lift distribution and the lowest drag among the trimmed stable designs. This was achieved by a combination of washout and reflex airfoils determined by the optimizer to be the best.

The optimized BWB at off-design flight conditions was also investigated by analyzing it for a range of Mach numbers while enforcing trim. The optimized design exhibited significantly lower drag over the entire transonic regime when compared to the baseline. In the optimized design, a low trim drag at high speeds and a high trim drag at low speeds was observed, which was the opposite of the baseline BWB trend.

In Study 5, the design space was further explored by adding wing planform design variables to the optimization while enforcing a center plane bending moment constraint. The addition of planform variables achieved an additional drag reduction. The optimized design increased the span by 3% and reduced the sweep angle by 4 deg. This demonstrated the benefit of simultaneously optimizing the planform and shape, and highlighted the importance of aerostructural considerations. One of these considerations is the structural weight increase incurred by increases in span or sweep, which were addressed by enforcing the bending moment constraint. Because the right value for constraint requires a full aerostructural optimization that is beyond the scope of this paper, the effect of varying the bending moment constraint on the optimal designs in Study 4 was investigated. The results showed that, when the bending moment constraint was reduced to 60% of the baseline value, the optimal design exhibited negative loading at the wingtips.

Finally, the effect of multipoint optimization was studied in Study 6. This resulted in a more robust design than that of the single-point optimization, as evidenced by the enlarged contour of the 99% maximum ML/D. The contours of ML/D for the twist-optimized baseline, single point optimum, and multipoint optimum were also compared. These contours showed that the maximum ML/D occurs at a lower cruise Mach number and higher C_L than the design flight conditions, indicating that the configuration should either fly higher or have a smaller planform area (although the engine performance would degrade with an altitude increase, and the planform area is probably constrained by field performance). Nevertheless, the aerodynamic shape optimization successfully moved the ML/D peak toward the design points, and flattened the peak in the multipoint case.

Given the results of these studies, the authors believe that RANS-based aerodynamic shape optimization has become a practical aircraft design tool that is especially useful for the design of BWB configurations. This type of optimization was enabled by the combination of a nonlinear constrained optimizer and an efficient computation of the aerodynamic force coefficient gradients with respect to hundreds of shape design variables. In the case of the BWB in particular, the optimal combination of wing twist, and airfoil reflex to obtain the lowest drag while satisfying trim, stability and structural constraints is not obvious, but numerical optimization can help designers find the best possible configuration.

References

[1] Liebeck, R. H., "Design of the Blended Wing Body Subsonic Transport," *Journal of Aircraft*, Vol. 41, No. 1, 2004, pp. 10–25.
doi:10.2514/1.9084

[2] Kroo, I., "Innovations in Aeronautics," *42nd AIAA Aerospace Sciences Meeting*, AIAA Paper 2004-0001, Jan. 2004.

[3] Qin, N., Vavalle, A., Le Moigne, A., Laban, M., Hackett, K., and Weinerfelt, P., "Aerodynamic Considerations of Blended Wing Body Aircraft," *Progress in Aerospace Sciences*, Vol. 40, No. 6, 2004, pp. 321–343.
doi:10.1016/j.paerosci.2004.08.001

[4] Roman, D., Gilmore, R., and Wakayama, S., "Aerodynamics of High-Subsonic Blended-Wing-Body Configurations," *41st Aerospace Sciences Meeting and Exhibit*, AIAA Paper 2003-0554, 2003.

[5] Liebeck, R., "Design of the Blended-Wing-Body Subsonic Transport," *40th AIAA Aerospace Sciences Meeting and Exhibit*, AIAA Paper 2002-0002, 2002.

[6] Wakayama, S., "Multidisciplinary Design Optimization of the Blended-Wing-Body," *7th AIAA Symposium on Multidisciplinary Analysis and Optimization*, AIAA Paper 1998-4938, 1998.

[7] Wakayama, S., "Blended-Wing-Body Optimization Problem Setup," *8th Symposium on Multidisciplinary Analysis and Optimization*, AIAA Paper 2000-4740, 2000.

[8] Qin, N., Vavalle, A., and Moigne, A. L., "Spanwise Lift Distribution for Blended Wing Body Aircraft," *Journal of Aircraft*, Vol. 42, No. 2, 2005, pp. 356–365.
doi:10.2514/1.4229

[9] Peigin, S., and Epstein, B., "Computational Fluid Dynamics Driven Optimization of Blended Wing Body Aircraft," *AIAA Journal*, Vol. 44, No. 11, 2006, pp. 2736–2745.
doi:10.2514/1.19757

[10] Kuntawala, N. B., Aerodynamic Shape Optimization of a Blended-Wing-Body Aircraft Configuration, Master's Thesis, Univ. of Toronto, Toronto, 2011.

[11] Kuntawala, N. B., Hicken, J. E., and Zingg, D. W., "Preliminary Aerodynamic Shape Optimization of a Blended-Wing-Body Aircraft Configuration," *49th AIAA Aerospace Sciences Meeting*, AIAA Paper 2011-0642, 2011.

[12] Meheut, M., Arntz, A., and Carrier, G., "Aerodynamic Shape Optimizations of a Blended Wing Body Configuration for Several Wing Planforms," *30th AIAA Applied Aerodynamics Conference*, AIAA Paper 2012-3122, 2012.

[13] Mader, C. A., and Martins, J. R. R. A., "Stability-Constrained Aerodynamic Shape Optimization of Flying Wings," *Journal of Aircraft*, Vol. 50, No. 5, 2013, pp. 1431–1449.
doi:10.2514/1.C031956

[14] Lyu, Z., and Martins, J. R. R. A., "Aerodynamic Shape Optimization of a Blended-Wing-Body Aircraft," *51st AIAA Aerospace Sciences Meeting Including the New Horizons Forum and Aerospace Exposition*, AIAA Paper 2013-0283, 2013.

[15] Lyu, Z., and Martins, J. R. R. A., "RANS-Based Aerodynamic Shape Optimization of a Blended-Wing-Body Aircraft," *43rd AIAA Fluid Dynamics Conference and Exhibit*, AIAA Paper 2013-2586, June 2013.

[16] Reist, T. A., and Zingg, D. W., "Aerodynamic Shape Optimization of a Blended-Wing-Body Regional Transport for a Short Range Mission," *31st AIAA Applied Aerodynamics Conference*, AIAA Paper 2013-2414, July 2013.

[17] Lyu, Z., Kenway, G., Paige, C., and Martins, J. R. R. A., "Automatic Differentiation Adjoint of the Reynolds-Averaged Navier–Stokes Equations with a Turbulence Model," *43rd AIAA Fluid Dynamics Conference and Exhibit*, AIAA Paper 2013-2581, June 2013.

[18] Kenway, G. K. W., Kennedy, G. J., and Martins, J. R. R. A., "A Scalable Parallel Approach for High-Fidelity Steady-State Aeroelastic Analysis and Adjoint Derivative Computations," *AIAA Journal* (in press). doi:10.2514/1.J052255.

[19] Kenway, G. K. W., and Martins, J. R. R. A., "Multi-Point High-Fidelity Aerostructural Optimization of a Transport Aircraft Configuration," *Journal of Aircraft*, Vol. 51, No. 1, 2014, pp. 144–160. doi:10.2514/1.C032150.

[20] Kenway, G. K., Kennedy, G. J., and Martins, J. R. R. A., "A CAD-Free Approach to High-Fidelity Aerostructural Optimization," *Proceedings of the 13th AIAA/ISSMO Multidisciplinary Analysis Optimization Conference*, AIAA Paper 2013-9231, 2010.

[21] Kota, S., Osborn, R., Ervin, G., Maric, D., Flick, P., and Paul, D., "Mission Adaptive Compliant Wing-Design, Fabrication and Flight Test," *RTO Applied Vehicle Technology Panel (AVT) Symposium*, Paper RTO-MP-AVT-168, 2009.

[22] van der Weide, E., Kalitzin, G., Schluter, J., and Alonso, J., "Unsteady Turbomachinery Computations Using Massively Parallel Platforms," *44th AIAA Aerospace Sciences Meeting and Exhibit*, AIAA Paper 2006-0421, 2006. doi:10.2514/6.2006-421

[23] Jameson, A., Schmidt, W., and Turkel, E., "Numerical Solution of the Euler Equations by Finite Volume Methods Using Runge Kutta Time Stepping Schemes," *14th AIAA, Fluid and Plasma Dynamics Conference*, AIAA Paper 1981-1259, 1981.

[24] Mader, C. A., Martins, J. R. R. A., Alonso, J. J., and van der Weide, E., "ADjoint: An Approach for the Rapid Development of Discrete Adjoint Solvers," *AIAA Journal*, Vol. 46, No. 4, 2008, pp. 863–873. doi:10.2514/1.29123

[25] Saad, Y., and Schultz, M. H., "GMRES: A Generalized Minimal Residual Algorithm for Solving Nonsymmetric Linear Systems," *SIAM Journal on Scientific and Statistical Computing*, Vol. 7, No. 3, 1986, pp. 856–869. doi:10.1137/0907058

[26] Balay, S., Gropp, W. D., McInnes, L. C., and Smith, B. F., "Efficient Management of Parallelism in Object Oriented Numerical Software Libraries," *Modern Software Tools in Scientific Computing*, edited by Bruaset, E., Arge, A. M., and Langtangen, H. P., Birkhäuser Press, Boston, 1997, pp. 163–202. doi:10.1007/978-1-4612-1986-6_8

[27] Balay, S., Brown, J., Buschelman, K., Eijkhout, V., Gropp, W. D., Kaushik, D., Knepley, M. G., McInnes, L. C., Smith, B. F., and Zhang, H., "PETSc Users Manual," Argonne National Laboratory, Tech. Rept. ANL-95/11 Revision 3.4, Lemont, IL, 2013.

[28] Gill, P. E., Murray, W., and Saunders, M. A., "SNOPT: An SQP Algorithm for Large-Scale Constrained Optimization," *SIAM Journal on Optimization*, Vol. 12, No. 4, 2002, pp. 979–1006. doi:10.1137/S1052623499350013

[29] Perez, R. E., Jansen, P. W., and Martins, J. R. R. A., "pyOpt: A Python-Based Object-Oriented Framework for Nonlinear Constrained Optimization," *Structures and Multidisciplinary Optimization*, Vol. 45, No. 1, 2012, pp. 101–118. doi:10.1007/s00158-011-0666-3

[30] Martins, J. R. R. A., and Lambe, A. B., "Multidisciplinary Design Optimization: A Survey of Architectures," *AIAA Journal*, Vol. 51, No. 9, 2013, pp. 2049–2075. doi:10.2514/1.J051895

[31] Mader, C. A., and Martins, J. R. R. A., "Computation of Aircraft Stability Derivatives Using an Automatic Differentiation Adjoint Approach," *AIAA Journal*, Vol. 49, No. 12, 2011, pp. 2737–2750. doi:10.2514/1.J051147

[32] Mader, C. A., and Martins, J. R. R. A., "Stability-Constrained Aerodynamic Shape Optimization of Flying Wings," *Journal of Aircraft*, Vol. 50, No. 5, Sep. 2013, pp. 1431–1449. doi:10.2514/1.C031956

[33] Haimes, R., "Automated Feature Extraction from Transient CFD Simulations," *Proceedings of the 7th Annual Conference of the CFD Society of Canada*, May 1999.

[34] Jones, R. T., "The Spanwise Distribution of Lift for Minimum Induced Drag of Wings Having a Given Lift and a Given Bending Moment," NASA TN-2249, Dec. 1950.

[35] Liem, R. P., Kenway, G. K., and Martins, J. R. R. A., "Multi-Point, Multi-Mission, High-Fidelity Aerostructural Optimization of a Long-Range Aircraft Configuration," *Proceedings of the 14th AIAA/ISSMO Multidisciplinary Analysis and Optimization Conference*, AIAA Paper 2012-5706, Sept. 2012.

[36] Torenbeek, E., *Advanced Aircraft Design: Conceptual Design, Technology and Optimization of Subsonic Civil Airplanes*, Aerospace Series, Wiley, New York, 2013, pp. 363–391. doi:10.1002/9781118568101